Time-Critical Cooperative Path Following of Multiple UAVs: Case Studies

Isaac Kaminer[1], Enric Xargay[2], Venanzio Cichella[2], Naira Hovakimyan[2], António Manuel Pascoal[3], A. Pedro Aguiar[4], Vladimir Dobrokhodov[1], and Reza Ghabcheloo[5]

[1] Naval Postgraduate School, Monterey, CA 93943, USA
{kaminer,vldobr}@nps.edu
[2] University of Illinois at Urbana-Champaign, Urbana, IL 61801, USA
{xargay,cichell2,nhovakim}@illinois.edu
[3] Instituto Superior Técnico, University of Lisbon, LX 1049-001, Portugal
antonio@isr.ist.utl.pt
[4] Faculty of Engineering, University of Porto, P.O. 4200, Portugal
pedro.aguiar@fe.up.pt
[5] Tampere University of Technology, Tampere, FI-33101, Finland
reza.ghabcheloo@tut.fi

Abstract. This paper describes a multi-vehicle motion control framework for time-critical cooperative missions and evaluates its performance by considering two case studies: a simultaneous arrival mission scenario and a sequential auto-landing of a fleet of UAVs. In the adopted setup, the UAVs are assigned nominal spatial paths and speed profiles along those paths; the vehicles are then tasked to execute cooperative path following, rather than "open-loop" trajectory tracking. This cooperative strategy yields robust behavior against external disturbances by allowing the UAVs to negotiate their speeds along the paths in response to information exchanged over a supporting communications network.

1 Introduction

Unmanned Aerial Vehicles (UAVs) are ubiquitous in military reconnaissance and strike operations, border patrol missions, forest fire detection, and recovery operations. In simple missions, a single vehicle can be managed by a crew using a ground station provided by the vehicle manufacturer. The execution of more challenging missions, however, requires the use of multiple vehicles working in cooperation to achieve a common objective. Such missions require vehicles to execute maneuvers in close proximity to each other, and to effectively exchange information so as to meet desired spatial and temporal constraints. The flow of information among vehicles is often severely restricted, either for security reasons or because of tight bandwidth limitations. A key enabling element for the execution of such missions is thus the availability of cooperative motion control strategies that can yield robust performance in the face of external disturbances and communications limitations, while ensuring collision-free maneuvers.

© Springer-Verlag Berlin Heidelberg 2015

D. Choukroun et al. (eds.), *Advances in Estimation, Navigation, and Spacecraft Control*,
DOI: 10.1007/978-3-662-44785-7_12

The range of relevant, related topics addressed in literature includes parallel computing [1], synchronization of oscillators [2], study of collective behavior and flocking [3], multi-system consensus mechanisms [4], multi-vehicle system formations [5–8], coordinated motion control [9–11], cooperative path and trajectory planning [12–15], asynchronous protocols [16], dynamic graphs [17], stochastic graphs [17–19], and graph-related theory [20,21]. Especially relevant are the applications of the theory developed in the area of multi-vehicle control: spacecraft formation flying [22], UAV control [23,24], coordinated control of land robots [9], and control of multiple autonomous marine vehicles [25–30]. In spite of significant progress in the field, much work remains to be done to develop strategies capable of providing guaranteed levels of performance in the presence of complex vehicle dynamics, communications constraints, and partial vehicle failures.

In [31], we addressed the problem of *steering a fleet of UAVs along desired spatial paths while meeting relative temporal constraints*. Representative examples of such missions are sequential auto-landing and coordinated ground target suppression; in both cases, only *relative* –rather than *absolute*– temporal constraints are given a priori. In the proposed framework, the vehicles are assigned nominal paths and speed profiles along those, obtained from an appropriately formulated optimization problem. The paths are judiciously parameterized, and the vehicles are requested to execute cooperative path following, rather than "open-loop" trajectory-tracking maneuvers. The reader is referred to [31–35] for a general perspective of key ideas that are at the root of this distributed cooperative approach. In the present paper, we present simulation results of two multi-vehicle time-critical missions that exploit the cooperative control framework developed in [31]. In the first mission, three UAVs must follow spatially-deconflicted paths and arrive at predefined locations at the same time. The second mission considers the case of sequential auto-landing, in which three UAVs must arrive at the glide path separated by prespecified safe-guarding time-intervals and maintain this separation as they fly along the glide slope.

The paper is organized as follows. Section 2 formulates the time-critical cooperative path-following problem and introduces a set of assumptions on the supporting network. Section 3 presents a path-following control algorithm for UAVs in 3D space. Section 4 derives a strategy for time-critical cooperative path following of multiple UAVs that relies on the adjustment of the speed profile of each vehicle. Section 5 presents simulation results that demonstrate the effectiveness of the algorithms. Finally, Section 6 summarizes concluding remarks.

The following notation is used throughout the paper. Uppercase calligraphic letters are used to denote reference frames, e.g. $\mathcal{F}$; $\{\boldsymbol{v}\}_F$ is used to denote vector $\boldsymbol{v}$ resolved in frame $\mathcal{F}$; $\{\hat{\boldsymbol{e}}\}_F$ represents versor $\hat{\boldsymbol{e}}$ resolved in frame $\mathcal{F}$; $\boldsymbol{\omega_{F1/F2}}$ denotes the angular velocity of frame $\mathcal{F}1$ with respect to frame $\mathcal{F}2$; the rotation matrix from frame $\mathcal{F}1$ to frame $\mathcal{F}2$ is represented by $\boldsymbol{R}_{\boldsymbol{F1}}^{\boldsymbol{F2}}$; $\dot{\boldsymbol{v}}\,]_F$ indicates that the time-derivative of vector $\boldsymbol{v}$ is taken in frame $\mathcal{F}$. The notation $\|\cdot\|$ is used for the 2-norm of a vector. Finally, $\mathsf{SO(3)}$ denotes the Special Orthogonal group of all rotations about the origin of three-dimensional Euclidean space $\mathbb{R}^3$, while $\mathfrak{so}(3)$ represents the set of 3×3 skew-symmetric matrices over $\mathbb{R}$.

2 Problem Formulation

This section formulates in a concise manner the problem of time-critical cooperative path-following control of multiple UAVs in 3D space, in which a fleet of UAVs is tasked to converge to and follow a set of desired feasible paths so as to meet spatial and temporal constraints. The section also introduces a set of assumptions and constraints on the supporting communications network.

We note that the problem of cooperative *trajectory generation* is not addressed in this paper. In fact, it is assumed that a set of desired 3D time-trajectories $\boldsymbol{p_{d,i}}(t_d) : [0, t_d^*] \to \mathbb{R}^3$, $i = 1, \ldots, n$, conveniently parameterized by a single time-variable t_d, is known for all the n UAVs involved in the mission. The variable t_d represents a *desired mission time* (distinct from the actual mission time that evolves as the mission unfolds), with t_d^* being the *desired mission duration*. For a given t_d, $\boldsymbol{p_{d,i}}(t_d)$ defines the desired position of the ith UAV t_d seconds after the initiation of the mission. These time-trajectories can be reparameterized in terms of arc length to obtain *spatial paths* $\boldsymbol{p_{d,i}}(\tau_{\ell,i}) : [0, \ell_{fi}] \to \mathbb{R}^3$ –with no temporal specifications– and the corresponding *desired speed profiles* $v_{d,i}(t_d) : [0, t_d^*] \to \mathbb{R}$. For convenience, each spatial path is parameterized by its arc length $\tau_{\ell,i}$, with ℓ_{fi} denoting the total length of the ith path, whereas the desired speed profiles are parameterized by the desired mission time t_d. It is assumed that both the paths and the speed profiles satisfy collision-avoidance constraints as well as appropriate boundary and feasibility conditions, such as those imposed by the physical limitations of the UAVs. The problem of generating feasible time-critical trajectories for multiple vehicles is described in [36, 37].

2.1 Path Following for a Single UAV

The solution to the path-following problem described in this paper extends the algorithm in [38] to the 3D case, and relies on the insight that a UAV can follow a given path using only its attitude, thus leaving its linear speed as a degree of freedom to be used at the coordination level. Following the approach developed in [38], this section introduces a *virtual target vehicle* running along the 3D path, defines a frame attached to this virtual target, and characterizes a generalized error vector between this moving coordinate system and a frame attached to the actual UAV. With this setup, the path-following problem is reduced to driving this generalized error vector to zero by using only the UAV's attitude control effectors, while following an arbitrary feasible speed profile.

Figure 1 captures the geometry of the problem at hand. The symbol $\mathcal{I}$ denotes an inertial reference frame $\{\hat{\mathbf{e}}_\mathbf{1}, \hat{\mathbf{e}}_\mathbf{2}, \hat{\mathbf{e}}_\mathbf{3}\}$ and $\boldsymbol{p_d}(\cdot)$ is the desired path assigned to one of the vehicles, with ℓ_f being its total path length. Vector $\boldsymbol{p_I}(t)$ denotes the position of the center of mass Q of the vehicle in this inertial frame. Further, we let P be an arbitrary point on the desired path that plays the role of the virtual target, and denote by $\boldsymbol{p_d}(\ell)$ its position in the inertial frame. Here $\ell \in [0, \ell_f]$ is a free length variable that defines the position of the virtual target vehicle along the path. In the setup adopted, the total rate of progression of the virtual target along the path, $\dot{\ell}(t)$, is an additional design parameter. Endowing point P with

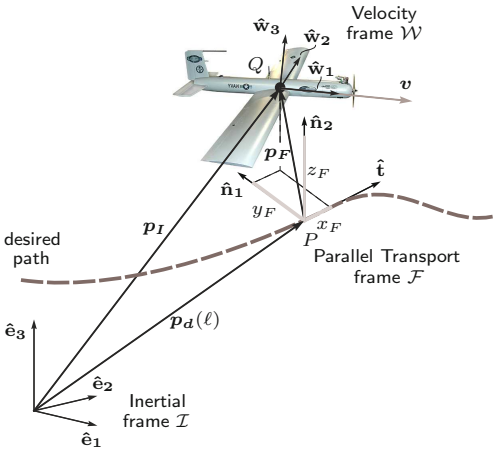

Fig. 1. Following a virtual target vehicle; problem geometry

an extra degree of freedom is the key to the path-following algorithm presented in [38] and its extension to the 3D case described in this paper.

For our purposes, it is convenient to define a *parallel transport frame* $\mathcal{F}$ [39] attached to point P on the path and characterized by vectors $\{\hat{\mathbf{t}}(\ell), \hat{\mathbf{n}}_\mathbf{1}(\ell), \hat{\mathbf{n}}_\mathbf{2}(\ell)\}$. These vectors define an orthonormal basis for $\mathcal{F}$, in which the unit vector $\hat{\mathbf{t}}(\ell)$ defines the tangent direction to the path at the point determined by ℓ, while $\hat{\mathbf{n}}_\mathbf{1}(\ell)$ and $\hat{\mathbf{n}}_\mathbf{2}(\ell)$ define the normal plane perpendicular to $\hat{\mathbf{t}}(\ell)$. Unlike the Frenet-Serret frame, parallel transport frames are well defined when the path has a vanishing second derivative. Moreover, let $\boldsymbol{p_F}(t)$ be the position of the vehicle's center of mass Q in this moving frame, and let $x_F(t)$, $y_F(t)$, and $z_F(t)$ be the components of vector $\boldsymbol{p_F}(t)$ with respect to the basis $\{\hat{\mathbf{t}}, \hat{\mathbf{n}}_\mathbf{1}, \hat{\mathbf{n}}_\mathbf{2}\}$.

Let $\mathcal{W}$ denote a vehicle-carried velocity frame $\{\hat{\mathbf{w}}_\mathbf{1}, \hat{\mathbf{w}}_\mathbf{2}, \hat{\mathbf{w}}_\mathbf{3}\}$ with its origin at the UAV center of mass and its x-axis aligned with the velocity vector of the UAV. The z-axis is chosen to lie in the plane of symmetry of the UAV, and the y-axis is determined by completing the right-hand system. In this paper, $q(t)$ and $r(t)$ are the y-axis and z-axis components, respectively, of the vehicle's rotational velocity resolved in the $\mathcal{W}$ frame. With a slight abuse of notation, $q(t)$ and $r(t)$ will be referred to as *pitch rate* and *yaw rate*, respectively.

We also introduce an auxiliary frame $\mathcal{D}$ defined by $\{\hat{\mathbf{b}}_\mathbf{1D}, \hat{\mathbf{b}}_\mathbf{2D}, \hat{\mathbf{b}}_\mathbf{3D}\}$, which is used to shape the approach attitude to the path as a function of the cross-track error components y_F and z_F. Frame $\mathcal{D}$ has its origin at the UAV center of mass and vectors $\hat{\mathbf{b}}_\mathbf{1D}(t)$, $\hat{\mathbf{b}}_\mathbf{2D}(t)$, and $\hat{\mathbf{b}}_\mathbf{3D}(t)$ are defined as

$$\hat{\mathbf{b}}_\mathbf{1D} := \frac{d\,\hat{\mathbf{t}} - y_F\,\hat{\mathbf{n}}_\mathbf{1} - z_F\,\hat{\mathbf{n}}_\mathbf{2}}{\left(d^2 + y_F^2 + z_F^2\right)^{\frac{1}{2}}} \quad , \qquad \hat{\mathbf{b}}_\mathbf{2D} := \frac{y_F\,\hat{\mathbf{t}} + d\,\hat{\mathbf{n}}_\mathbf{1}}{\left(d^2 + y_F^2\right)^{\frac{1}{2}}} \quad , \qquad \hat{\mathbf{b}}_\mathbf{3D} := \hat{\mathbf{b}}_\mathbf{1D} \times \hat{\mathbf{b}}_\mathbf{2D} \quad ,$$

with $d > 0$ being a constant *characteristic distance* that plays the role of a design parameter. The basis vector $\hat{\mathbf{b}}_\mathbf{1D}(t)$ defines the desired direction of the UAV's velocity vector. Clearly, when the vehicle is far from the desired path,

vector $\hat{\mathbf{b}}_{\mathbf{1D}}(t)$ becomes perpendicular to $\hat{\mathbf{t}}(\ell)$. As the vehicle comes closer to the path and the cross-track error becomes smaller, vector $\hat{\mathbf{b}}_{\mathbf{1D}}(t)$ tends to $\hat{\mathbf{t}}(\ell)$.

Finally, let $\tilde{\boldsymbol{R}}(t) \in \mathsf{SO(3)}$ be the rotation matrix from $\mathcal{W}$ to $\mathcal{D}$, that is,

$$\tilde{\boldsymbol{R}} := \boldsymbol{R}_{\boldsymbol{W}}^{\boldsymbol{D}} = \boldsymbol{R}_{\boldsymbol{F}}^{\boldsymbol{D}}\, \boldsymbol{R}_{\boldsymbol{W}}^{\boldsymbol{F}} = (\boldsymbol{R}_{\boldsymbol{D}}^{\boldsymbol{F}})^{\top}\, \boldsymbol{R}_{\boldsymbol{W}}^{\boldsymbol{F}} \ ,$$

and define the real-valued attitude error function on $\mathsf{SO(3)}$

$$\Psi(\tilde{\boldsymbol{R}}) := \tfrac{1}{2}\mathrm{tr}\big[\big(\mathbb{I}_{\mathbf{3}} - \boldsymbol{\Pi}_{\boldsymbol{R}}^{\top}\boldsymbol{\Pi}_{\boldsymbol{R}}\big)\big(\mathbb{I}_{\mathbf{3}} - \tilde{\boldsymbol{R}}\big)\big] \ , \tag{1}$$

where $\boldsymbol{\Pi}_{\boldsymbol{R}}$ is defined as $\boldsymbol{\Pi}_{\boldsymbol{R}} := \left[\begin{smallmatrix} 0 & 1 & 0 \\ 0 & 0 & 1 \end{smallmatrix}\right]$. The function $\Psi(\tilde{\boldsymbol{R}})$ in (1) can be expressed in terms of the entries of $\tilde{\boldsymbol{R}}(t)$ as $\Psi(\tilde{\boldsymbol{R}}) = (1/2)(1 - \tilde{R}_{11})$, where $\tilde{R}_{11}(t)$ denotes the $(1,1)$ entry of $\tilde{\boldsymbol{R}}(t)$. Therefore, $\Psi(\tilde{\boldsymbol{R}})$ is a positive-definite function about $\tilde{R}_{11} = 1$. Note that $\tilde{R}_{11} = 1$ corresponds to the situation where the velocity vector of the UAV is aligned with the basis vector $\hat{\mathbf{b}}_{\mathbf{1D}}(t)$.

With the above notation, as shown in [31], the path-following kinematic-error dynamics between the UAV and its virtual target vehicle can be written as

$$\dot{\boldsymbol{p}}_{\boldsymbol{F}}]_F = -\ \dot{\ell}\,\hat{\mathbf{t}} \ -\ \boldsymbol{\omega}_{\boldsymbol{F/I}} \times \boldsymbol{p}_{\boldsymbol{F}} \ +\ v\,\hat{\mathbf{w}}_{\mathbf{1}} \ , \tag{2a}$$

$$\dot{\Psi}(\tilde{\boldsymbol{R}}) = \boldsymbol{e}_{\tilde{\boldsymbol{R}}} \cdot \left(\begin{bmatrix} q \\ r \end{bmatrix} - \boldsymbol{\Pi}_{\boldsymbol{R}} \tilde{\boldsymbol{R}}^{\top} \left(\boldsymbol{R}_{\boldsymbol{F}}^{\boldsymbol{D}} \{\boldsymbol{\omega}_{\boldsymbol{F/I}}\}_F + \{\boldsymbol{\omega}_{\boldsymbol{D/F}}\}_D \right) \right) \ , \tag{2b}$$

where $v(t)$ denotes the magnitude of the UAV's ground velocity vector and $\boldsymbol{e}_{\tilde{\boldsymbol{R}}}(t)$ is the attitude kinematic-error vector defined as

$$\boldsymbol{e}_{\tilde{\boldsymbol{R}}} := \tfrac{1}{2}\boldsymbol{\Pi}_{\boldsymbol{R}} \left(\left(\mathbb{I}_{\mathbf{3}} - \boldsymbol{\Pi}_{\boldsymbol{R}}^{\top}\boldsymbol{\Pi}_{\boldsymbol{R}}\right) \tilde{\boldsymbol{R}} - \tilde{\boldsymbol{R}}^{\top} \left(\mathbb{I}_{\mathbf{3}} - \boldsymbol{\Pi}_{\boldsymbol{R}}^{\top}\boldsymbol{\Pi}_{\boldsymbol{R}}\right) \right)^{\vee} \ ,$$

where $(\cdot)^{\vee} : \mathfrak{so}(3) \to \mathbb{R}^3$ denotes the *vee map* (see Appendix). In the kinematic-error model (2), $q(t)$ and $r(t)$ play the role of control inputs, while the rate of progression $\dot{\ell}(t)$ of point P along the path becomes an extra variable that can be manipulated at will. At this point, the path-following generalized error vector $\boldsymbol{x}_{\boldsymbol{pf}}(t)$ can be formally defined as

$$\boldsymbol{x}_{\boldsymbol{pf}} := \big[\, \boldsymbol{p}_{\boldsymbol{F}}^{\top} \,,\, \boldsymbol{e}_{\tilde{\boldsymbol{R}}}^{\top} \,\big]^{\top} \ .$$

Notice that, within the region where $\Psi(\tilde{\boldsymbol{R}}) < 1$, if $\boldsymbol{x}_{\boldsymbol{pf}} = 0$, then both the path-following position error and the path-following attitude error are equal to zero, that is, $\boldsymbol{p}_{\boldsymbol{F}} = \mathbf{0}$ and $\Psi(\tilde{\boldsymbol{R}}) = 0$.

Using the above formulation, and given a spatially defined feasible path $\boldsymbol{p}_{\boldsymbol{d}}(\cdot)$, the problem of path following for a single vehicle can now be defined accordingly.

Definition 1 (Path-Following Problem). *For a given UAV, design feedback control laws for pitch rate $q(t)$, yaw rate $r(t)$, and rate of progression $\dot{\ell}(t)$ of the virtual target along the path such that the path-following generalized error vector $\boldsymbol{x}_{\boldsymbol{pf}}(t)$ converges to a neighborhood of the origin with a guaranteed rate of convergence, regardless of the (feasible) temporal assignments of the mission.*

2.2 Time-Critical Coordination and Network Model

To enforce the temporal constraints of the mission, we formulate a consensus problem, in which the objective of the fleet of vehicles is to reach agreement on some distributed variables of interest. Appropriate coordination variables need thus to be defined that capture the temporal assignments of the mission.

For this purpose, let $\ell'_{d,i}(t_d)$ be the desired normalized curvilinear abscissa of the ith UAV along its path at the desired mission time t_d, which is given by

$$\ell'_{d,i}(t_d) := \tfrac{1}{\ell_{fi}} \int_0^{t_d} v_{d,i}(\tau)\, d\tau \ .$$

The trajectory-generation algorithm ensures that the desired speed profiles $v_{d,i}(\cdot)$ satisfy feasibility conditions, which implies that the following bounds hold:

$$0 < v_{\min} \leq v_{d,i}(\cdot) \leq v_{\max} \ , \qquad i = 1, \ldots, n \ , \tag{3}$$

where $v_{\min}$ and $v_{\max}$ denote, respectively, minimum and maximum operating speeds of the UAVs involved in the mission. From the definition of $\ell'_{d,i}(t_d)$ and the bounds in (3), it follows that $\ell'_{d,i}(t_d)$ is a strictly increasing continuous function of t_d mapping $[0, t_d^*]$ onto $[0, 1]$. Let $\eta_i : [0, 1] \to [0, t_d^*]$ be the inverse function of $\ell'_{d,i}(t_d)$. Clearly, $\eta_i(\cdot)$ is also a strictly increasing continuous function of its argument. Then, letting $\ell'_i(t) := \ell_i(t)/\ell_{fi}$, we introduce the time-variables

$$\xi_i(t) := \eta_i(\ell'_i(t)) \ , \qquad i = 1, \ldots, n \ .$$

Note that, for any two vehicles i and j, if $\xi_i(t) = \xi_j(t) = t'_d$ at a given time t, then $\ell'_i(t) = \ell'_{d,i}(t'_d)$ and $\ell'_j(t) = \ell'_{d,j}(t'_d)$, which implies that at time t the target vehicles corresponding to UAVs i and j have the desired relative position at the desired mission time t'_d. Moreover, if $\dot{\xi}_i(t) = 1$, then at time t the ith virtual target travels at the desired speed, $\dot{\ell}_i(t) = v_{d,i}(\xi_i(t))$. The variables $\xi_i(t)$ represent thus an appropriate measure of vehicle coordination and will be referred to as *coordination states*, while the functions $\eta_i(\cdot)$ will be called *coordination maps*.

To reach agreement on these coordination states, the UAVs need to exchange information over the supporting communications network. Next, tools and facts from *algebraic graph theory* [40] are used to model the information exchange over the network as well as the constraints imposed by the communications topology.

First, it is assumed that the ith UAV can only exchange information with a neighboring set of vehicles, denoted by $\mathcal{N}_i(t)$. It is also assumed that communications are bidirectional and, for simplicity, that information is transmitted continuously with no delays. Moreover, each vehicle is only allowed to exchange its coordination state $\xi_i(t)$ with its neighbors. Finally, we assume that the connectivity of the graph $\Gamma(t)$ that captures the underlying communications topology of the fleet at time t satisfies the persistency of excitation (PE)-like condition [41]

$$\frac{1}{n}\frac{1}{T}\int_t^{t+T} \boldsymbol{Q}\, \boldsymbol{L}(\tau)\, \boldsymbol{Q}^\top d\tau \geq \mu\, \mathbb{I}_{\boldsymbol{n-1}} \ , \qquad \text{for all } t \geq 0 \ , \tag{4}$$

where $\boldsymbol{L}(t) \in \mathbb{R}^{n \times n}$ is the Laplacian of the graph $\Gamma(t)$, and $\boldsymbol{Q}$ is an $(n-1) \times n$ matrix such that $\boldsymbol{Q}\mathbf{1}_{\boldsymbol{n}} = \mathbf{0}$ and $\boldsymbol{Q}\boldsymbol{Q}^\top = \mathbb{I}_{\boldsymbol{n-1}}$, with $\mathbf{1}_{\boldsymbol{n}}$ being the vector in $\mathbb{R}^n$

whose components are all 1. Parameters $T > 0$ and $\mu \in (0, 1]$ characterize the *quality of service* (QoS) of the communications network, which in the context of this paper represents a measure of the level of connectivity of the communications graph. Note that the PE-like condition (4) requires the communications graph $\Gamma(t)$ to be connected only in an integral sense, not pointwise in time. In fact, the graph may be disconnected during some interval of time or may even fail to be connected at all times.

Using the formulation above, one can now define the problem of time-critical cooperative path following for a fleet of n UAVs.

Definition 2 (Time-Critical Cooperative Path-Following Problem). *Given a fleet of n vehicles supported by an inter-vehicle communications network and a set of desired 3D time trajectories $\boldsymbol{p_{d,i}}(t_d)$, design feedback control laws for pitch rate $q_i(t)$, yaw rate $r_i(t)$, and speed $v_i(t)$ for all vehicles such that*

1. *for each vehicle i, $i = 1, \ldots, n$, the path-following error vector $\boldsymbol{x_{pf,i}}(t)$ converges to a neighborhood of the origin; and*
2. *for each pair of vehicles i and j, $i, j = 1, \ldots, n$, the coordination errors $(\xi_i(t) - \xi_j(t))$ and $(\dot{\xi}_i(t) - 1)$ converge to a neighborhood of the origin.*

3 3D Path Following Control law

To solve the path-following problem described in Sect. 2.2.1, we first let the rate of progression of point P along the path be governed by

$$\dot{\ell} = (v\, \hat{\mathbf{w}}_{\mathbf{1}} + k_\ell \boldsymbol{p_F}) \cdot \hat{\mathbf{t}} \ , \qquad k_\ell > 0 \ . \tag{5}$$

Then, the rate commands $q_c(t)$ and $r_c(t)$ given by

$$\begin{bmatrix} q_c \\ r_c \end{bmatrix} := \boldsymbol{\Pi_R} \tilde{\boldsymbol{R}}^\top \left(\boldsymbol{R_F^D} \{\boldsymbol{\omega_{F/I}}\}_F + \{\boldsymbol{\omega_{D/F}}\}_D \right) \ - \ 2k_{\tilde{R}} \boldsymbol{e_{\tilde{R}}} \ , \qquad k_{\tilde{R}} > 0 \ , \tag{6}$$

drive the path-following generalized error vector $\boldsymbol{x_{pf}}(t)$ to a neighborhood of zero with a guaranteed rate of convergence. More precisely, it can be shown that if the speed of the vehicle satisfies $0 < v_{\min} \leq v(t) \leq v_{\max}$, then the origin of the kinematic-error dynamics (2) with the controllers $q_c(t)$ and $r_c(t)$ in (6) is locally exponentially stable. A formal statement of this result can be found in [31], while insights into this path-following algorithm can be found in [36].

The use of the Special Orthogonal group $\mathsf{SO(3)}$ in the formulation of the attitude control problem avoids the geometric singularities and complexities that appear when dealing with local parameterizations of the vehicle's attitude. See, for example, the path-following control algorithm reported in [35].

Finally, we notice that the path-following control laws $q_c(t)$ and $r_c(t)$ represent outer-loop guidance commands to be tracked by the UAV. In this sense, the proposed solution departs from standard backstepping techniques in that the final path-following control laws can be seamlessly tailored to vehicles that are equipped with commercial autopilots.

4 Time-Critical Coordination

We now address the problem of time-critical cooperative path-following control of multiple vehicles. To this effect, the speeds of the UAVs are adjusted based on coordination information exchanged among the vehicles over the supporting communications network. The distributed coordination control law described next is intended to provide a correction to the desired speed profile $v_{d,i}(\cdot)$ obtained in the trajectory-generation step, and to generate a speed command $v_{c,i}(t)$. This speed command is then to be tracked by the ith vehicle to achieve coordination.

4.1 Distributed Coordination Law

We start by noting that the evolution of the ith coordination state is given by

$$\dot{\xi}_i = \frac{\dot{\ell}_i}{v_{d,i}(\xi_i)} \ .$$

Recalling from the solution to the path-following problem that the evolution of the ith virtual target vehicle is described by $\dot{\ell}_i = (v_i\, \hat{\mathbf{w}}_{\mathbf{1},\boldsymbol{i}} + k_\ell\, \boldsymbol{p}_{\boldsymbol{F},\boldsymbol{i}}) \cdot \hat{\mathbf{t}}_{\boldsymbol{i}}$, where for simplicity we have kept k_ℓ without indexing, the dynamics of the ith coordination state can be rewritten as

$$\dot{\xi}_i = \frac{(v_i\, \hat{\mathbf{w}}_{\mathbf{1},\boldsymbol{i}} + k_\ell\, \boldsymbol{p}_{\boldsymbol{F},\boldsymbol{i}}) \cdot \hat{\mathbf{t}}_{\boldsymbol{i}}}{v_{d,i}(\xi_i)} \ .$$

Then, to solve the time-coordination problem we use dynamic inversion and define the speed command for the ith vehicle as

$$v_{c,i} := \frac{u_{\text{coord},i}\, v_{d,i}(\xi_i) - k_\ell\, \boldsymbol{p}_{\boldsymbol{F},\boldsymbol{i}} \cdot \hat{\mathbf{t}}_{\boldsymbol{i}}}{\hat{\mathbf{w}}_{\mathbf{1},\boldsymbol{i}} \cdot \hat{\mathbf{t}}_{\boldsymbol{i}}} \ , \tag{7}$$

where $u_{\text{coord},i}(t)$ is a coordination control law to be defined later. With this speed command, the coordination dynamics for the ith target vehicle become

$$\dot{\xi}_i = u_{\text{coord},i} + \tfrac{e_{v,i}}{v_{d,i}(\xi_i)}\, \hat{\mathbf{w}}_{\mathbf{1},\boldsymbol{i}} \cdot \hat{\mathbf{t}}_{\boldsymbol{i}} \ ,$$

where $e_{v,i}(t) := v_i(t) - v_{c,i}(t)$ denotes the speed tracking error for the ith UAV.

Recall now that each UAV is allowed to exchange its coordination state $\xi_i(t)$ only with its neighbors $\mathcal{N}_i(t)$, which are defined by the communications topology. To observe this constraint, the following distributed coordination control law is proposed:

$$u_{\text{coord},1}(t) = -k_P \textstyle\sum_{j\in\mathcal{N}_1} (\xi_1(t) - \xi_j(t)) + 1 \ , \tag{8a}$$

$$u_{\text{coord},i}(t) = -k_P \textstyle\sum_{j\in\mathcal{N}_i} (\xi_i(t) - \xi_j(t)) + \chi_{I,i}(t) \ , \qquad i = 2,\ldots,n \ , \tag{8b}$$

$$\dot{\chi}_{I,i}(t) = -k_I \textstyle\sum_{j\in\mathcal{N}_i} (\xi_i(t) - \xi_j(t)) \, , \qquad \chi_{I,i}(0) = 1 \ , \quad i = 2,\ldots,n \ , \tag{8c}$$

where vehicle 1 is elected as the formation leader (which can be a *virtual vehicle*), and k_P and k_I are positive coordination control gains. Note that the coordination control law has a proportional-integral structure, which provides disturbance rejection capabilities at the coordination level [42].

4.2 Overall Time-Critical Cooperative Path-Following System

Figure 2 shows the overall cooperative path-following control architecture for the ith vehicle. With the approach adopted, the control architecture exhibits a multiloop control structure in which an inner-loop controller stabilizes the vehicle dynamics, while guidance outer-loop controllers are designed to control the vehicle kinematics, providing path-following and coordination capabilities.

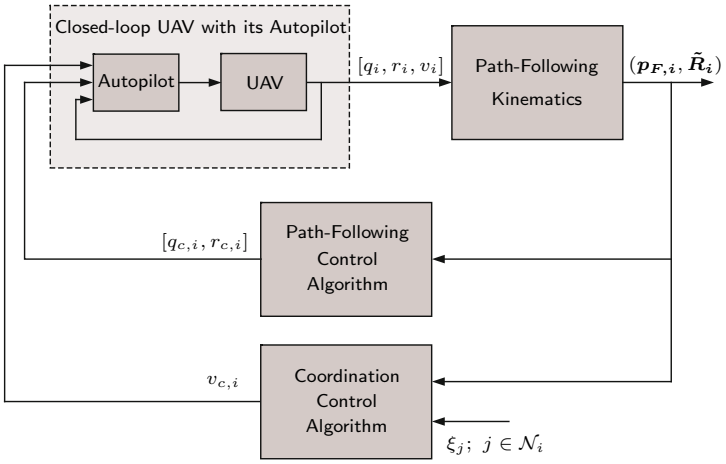

Fig. 2. Coordinated path-following closed-loop for the ith vehicle

It is proven in [31] that, if the connectivity of the communications graph verifies the PE-like condition (4) and the initial conditions are within a given domain of attraction, then there exist control gains for the path-following control law (5)-(6) and the coordination control law (7)-(8) that solve the time-critical cooperative path-following problem with guaranteed rates of exponential convergence, while ensuring at the same time that the speed of each UAV satisfies $v_{\min} \leq v_i(t) \leq v_{\max}$ for all $t \geq 0$.

Additionally, it is shown in [31] that the QoS of the network, characterized by parameters T and μ, limits the guaranteed rate of convergence of the coordination-error dynamics. The results in this paper also imply that, as the communications graph becomes connected pointwise in time, the convergence rate of the coordination-error dynamics can be set arbitrarily high by increasing the coordination control gains. This fact is consistent with results obtained in previous work; see [43, Lemma 2].

Finally, we notice that similar results have been derived for the case of a coordination control law with multiple leaders [42]; in this case, the convergence rate of the coordination dynamics depends not only on the QoS of the network, but also on the number of leaders. The work reported in [42] also analyzes the convergence properties of control law (8) when the vehicles exchange quantized information, and proves the existence of undesirable "zero-speed" attractors in the presence of coarse quantization.

5 Simulation Results

This section presents simulation results of two cooperative multi-vehicle mission scenarios that show the efficacy of the cooperative framework in this paper. In the first mission, three UAVs must execute a coordinated maneuver to arrive at predefined positions at the same time. We then consider a second mission in which three UAVs must execute sequential auto-landing while maintaining a prespecified safe-guarding separation along the glide slope. Both missions are designed to be executed by small tactical UAVs equipped with an autopilot providing angular-rate and speed tracking capabilities; see Fig. 3.

Fig. 3. SIG Rascal 110 research aircraft operated by the Naval Postgraduate School for time-critical cooperative missions. Onboard avionics include the Piccolo Plus autopilot, two PC-104 industrial embedded computers, and a wireless MANET link for air-to-air and air-to-ground communications. (See [36] for a detailed description of these avionics.)

5.1 Path-Following with Simultaneous Arrival

In this mission scenario, three UAVs are tasked to converge to and follow three spatially-deconflicted paths and arrive at their final destinations at the same time. A representative example of such mission is simultaneous suppression of multiple targets located at different positions. Note that this mission imposes only *relative* temporal constraints on the arrival of the UAVs.

Figure 4 shows the three paths with the parallel transport frames as well as the corresponding desired speed profiles, which assume a final desired speed of 20 m/s for all UAVs. The beginning of each path is indicated in this figure with a circle. The figure also shows the coordination maps η_i relating the desired normalized curvilinear abscissa $\ell'_{d,i}$ to the desired mission time t_d. The paths have lengths $\ell_{f1} = 2,084.8$ m, $\ell_{f2} = 1,806.4$ m, and $\ell_{f3} = 2,221.0$ m, and the desired time of arrival is $t_d^* = 85.0$ s. Figure 5 presents the path separations, which show a minimum spatial clearance of 125 m, and the desired inter-vehicle separations for this particular mission.

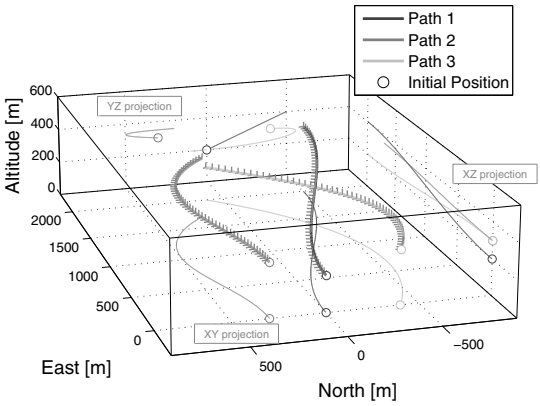

(a) Framed 3D paths

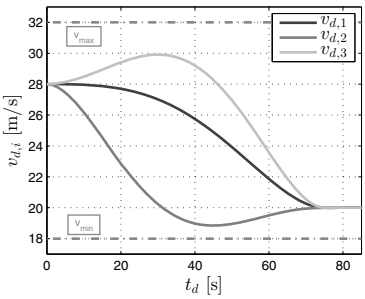

(b) Desired speed profiles

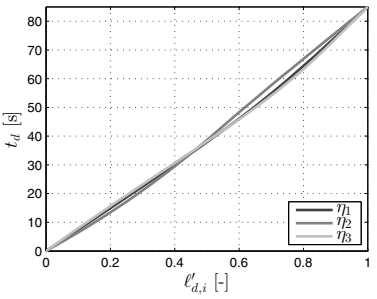

(c) Coordination maps

Fig. 4. Path-following with simultaneous arrival. Framed 3D spatial paths along with the corresponding desired speed profiles and coordination maps.

The cooperative motion-control algorithms described in this paper are used to solve this multi-vehicle simultaneous-arrival path-following problem. In order to achieve coordination, the UAVs rely on a supporting communications network. The information flow is assumed to be time-varying and, at any given time t, is characterized by one of the graphs in Fig. 6.

Simulation results for this particular mission are presented next. Figure 7 illustrates the evolution of the UAVs (black) as well as the virtual targets (mid gray) moving along the paths (light gray). This figure also includes the $\mathcal{W}$ frame attached to each UAV (black) as well as the $\mathcal{F}$ frame attached to the virtual targets (mid gray). The UAVs start the mission with an initial offset in both position and attitude with respect to the beginning of the framed paths. As can be seen in the figure, the path-following algorithm eliminates this initial offset and steers the UAVs along the corresponding paths, while the coordination algorithm ensures simultaneous arrival at the end of the path at $t = 84.2$ s.

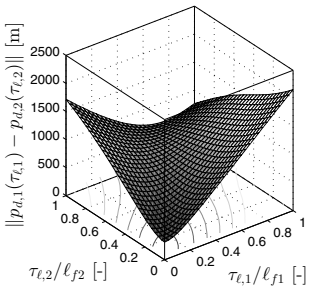

(a) Separation between paths 1 and 2

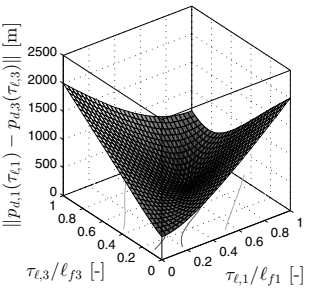

(b) Separation between paths 1 and 3

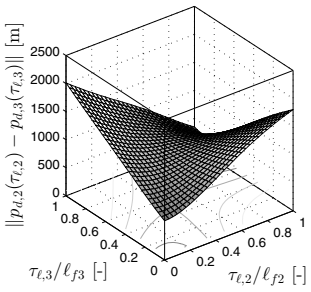

(c) Separation between paths 2 and 3

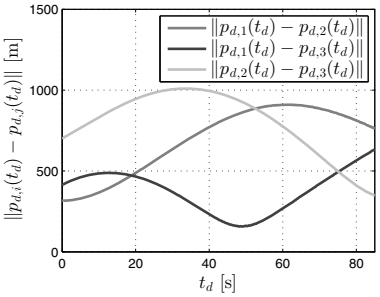

(d) Desired inter-vehicle separation

Fig. 5. Path-following with simultaneous arrival. Path separation and desired inter-vehicle separation; the three paths are spatially deconflicted with a minimum clearance of 125 m.

(a) Topology 1 (b) Topology 2 (c) Topology 3 (d) Topology 4

(e) Topology 5 (f) Topology 6 (g) Topology 7 (h) Topology 8

Fig. 6. Network topologies. At any given time t, the dynamic information flow is characterized by one of these graphs.

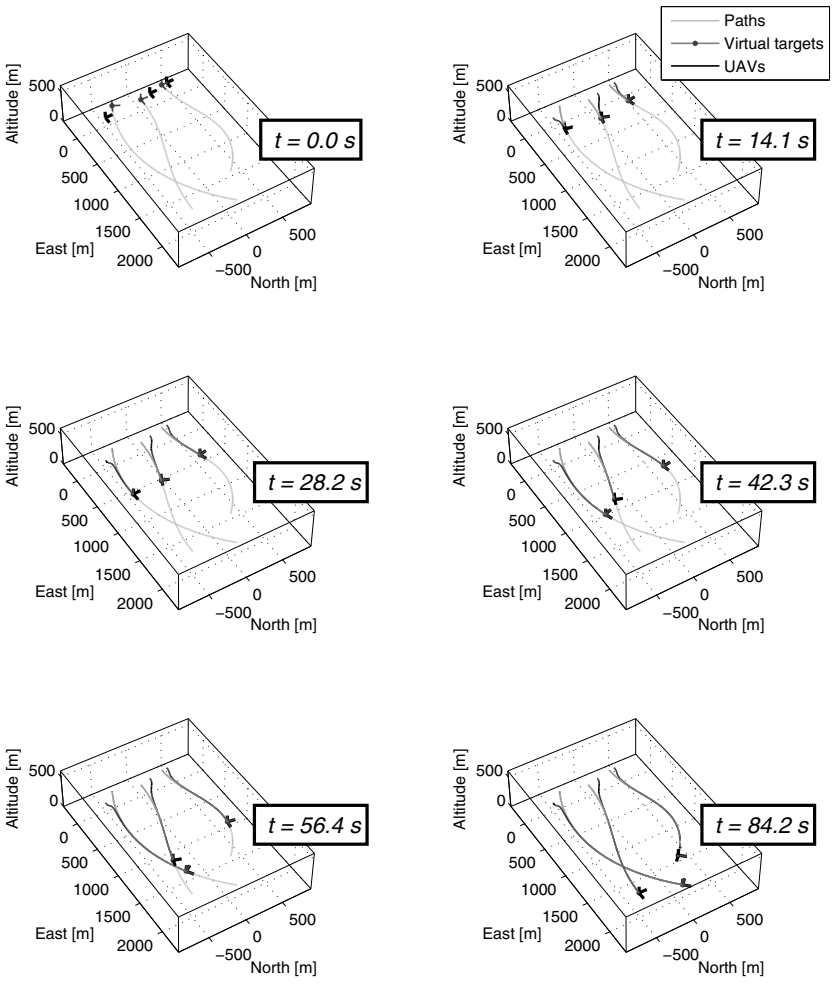

Fig. 7. Path-following with simultaneous arrival. The three UAVs achieve simultaneous arrival at their final destinations at $t = 84.2$ s.

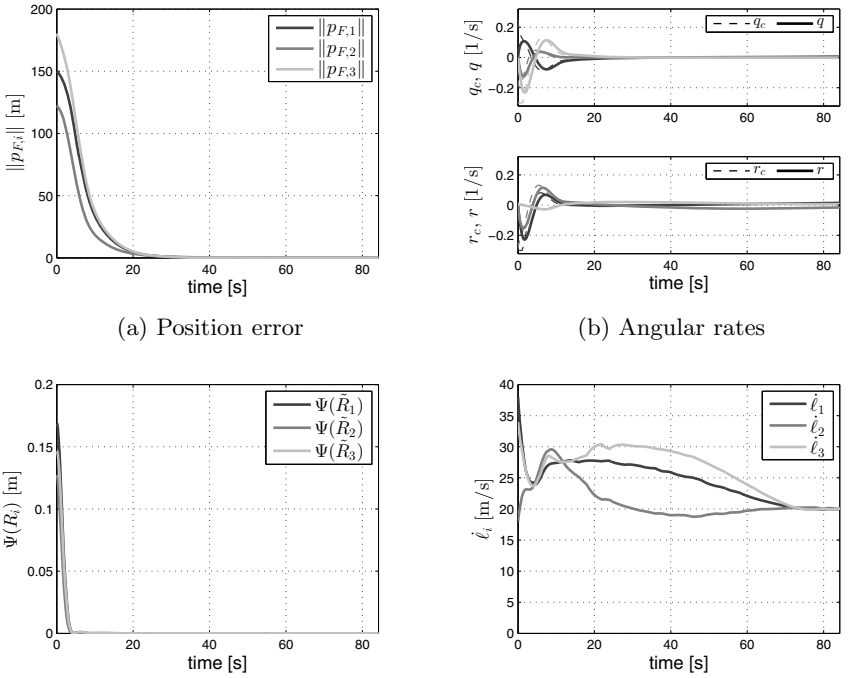

(a) Position error

(b) Angular rates

(c) Attitude error

(d) Progression of the virtual targets

Fig. 8. Path-following with simultaneous arrival. The path-following algorithm drives the path-following position and attitude errors to a neighborhood of zero.

Details about the performance of the path-following algorithm are shown in Fig. 8; the path-following position and attitude errors, $\boldsymbol{p_{F,i}}$ and $\Psi(\tilde{\boldsymbol{R}}_{\boldsymbol{i}})$, converge to a neighborhood of zero within 30 s. The figure also presents the angular-rate commands, $q_{c,i}$ and $r_{c,i}$, as well as the rate of progression $\dot{\ell}_i$ of the virtual targets along the path.

The evolution of both the coordination errors $(\xi_i - \xi_j)$ and the rate of change of the coordination states $\dot{\xi}_i$ are illustrated in Fig. 9, along with the resulting UAV speeds and the integral states implemented on the follower vehicles. The figure shows that the coordination errors converge to a neighborhood of zero, while the rate of change of the coordination states converges to the desired rate $\dot{\xi}_{\text{ref}} = 1$. In particular, Figure 9b illustrates how the vehicles adjust their speeds (with respect to the desired speed profile) to achieve coordination. Finally, Figure 10 describes the evolution of the information flow as the mission unfolds, and presents an estimate of the QoS of the network, computed as

$$\hat{\mu}(t) := \lambda_{\min}\left(\frac{1}{3}\frac{1}{T}\int_{t-T}^{t} \boldsymbol{Q_3 L}(\tau)\boldsymbol{Q_3}^{\top} d\tau\right) \ , \qquad t \geq T \ , \tag{9}$$

with $T = 10$ s.

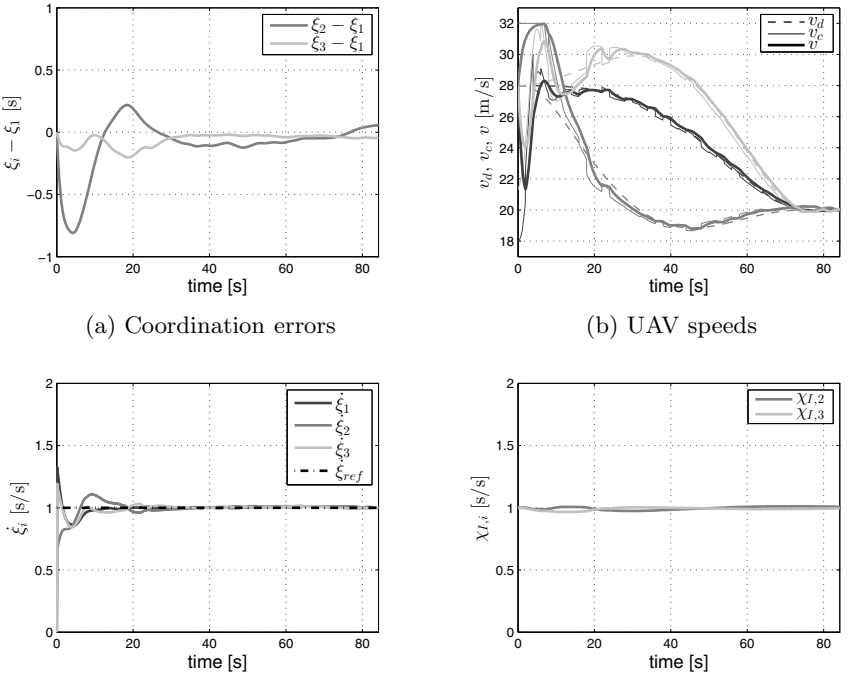

(a) Coordination errors

(b) UAV speeds

(c) Coordination-state rates

(d) Integral states

Fig. 9. Path-following with simultaneous arrival. The coordination control law ensures that the coordination errors converge to a neighborhood of zero and also that the rate of change of the coordination states evolves at about the desired rate $\dot{\xi}_{\mathrm{ref}} = 1$.

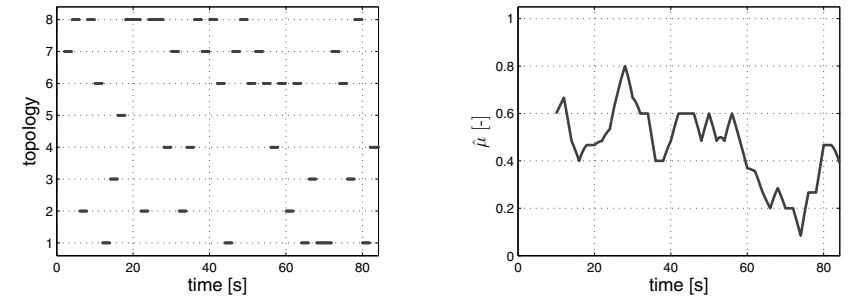

(a) Topology

(b) QoS estimate

Fig. 10. Path-following with simultaneous arrival. At a given time instant, the information flow is characterized by one of the topologies in Fig. 6. The resulting graph is only connected in an integral sense, and not pointwise in time.

5.2 Sequential Auto-Landing

Here, three UAVs must arrive at the assigned glide slope separated by prespecified safe-guarding time-intervals, and then follow the glide path at a constant approach speed while maintaining the safe-guarding separation. To this end, time-deconflicted transition trajectories are generated from prespecified initial conditions to the beginning of the glide path, satisfying the desired inter-vehicle arrival schedule and taking the UAVs to the desired approach speed. Again, this mission imposes only *relative* temporal constraints on the arrival of the UAVs.

Figure 11 shows the three transition paths with the parallel transport frames as well as the framed 3-deg glide path. The beginning of each transition path is indicated with a circle, while the beginning of the glide path is indicated with a triangle. The figure also presents the desired speed profiles for the initial transition phase that ensure a desired safe-guarding arrival separation of 30 s, trajectory deconfliction, as well as a final approach speed of 20 m/s. The transition coordination maps are shown in Fig. 11c. Finally, the figure also includes the desired speed profile for the approach along the glide slope as well as the corresponding coordination map. The transition paths have lengths $\ell_{f1} = 1,609.0$ m, $\ell_{f2} = 1,962.7$ m, and $\ell_{f3} = 2,836.7$ m, and the desired times of arrival at the glide slope are $t^*_{d1} = 65.0$ s, $t^*_{d2} = 95.0$ s, and $t^*_{d3} = 125.0$ s. Figure 12 presents the path separations, which show that the three transition paths meet at their end positions (beginning of the glide slope), whereas the desired inter-vehicle separations for this particular mission are never less than 350 m.

The cooperative motion-control algorithms described in this paper can be used to solve this sequential auto-landing problem. In this case, however, since the UAVs are required to maintain a safe-guarding separation during the approach along the glide path, the coordination states have to be redefined as the vehicles reach the glide slope. Hence, while the ith UAV is flying along its transition path, its coordination state is defined as

$$\xi_i(t) = \eta_i(\ell'_i(t)) \ , \qquad i = 1, 2, 3 \ ,$$

where $\ell'_i(t)$ is the normalized curvilinear abscissa of the ith virtual target along the corresponding transition path. When the UAV reaches the beginning of the glide path, then its coordination state is (re)defined as

$$\xi_i(t) = \eta_{\rm gs}(\ell'_i(t)) + t^*_{di} \ , \qquad i = 1, 2, 3 \ ,$$

where $\ell'_i(t)$ is now the normalized curvilinear abscissa of the ith virtual target along the glide path, and t^*_{di} is the desired time of arrival of the ith UAV at the beginning of the glide slope. Note that, with the above definitions, the coordination states $\xi_i(t)$ are continuous, as $\eta_i(1) = t^*_{di}$ and $\eta_{\rm gs}(0) = 0$.

Next, we present simulation results for this mission scenario. Figure 13 illustrates the evolution of the UAVs (black) as well as the virtual targets (mid gray) moving along the paths (light gray). Similar to the previous scenario, the

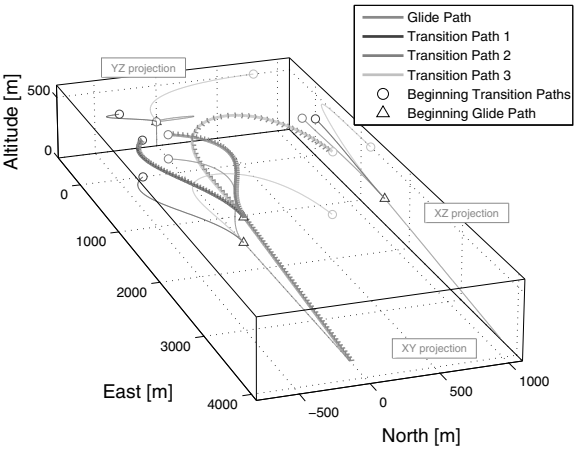

(a) Framed 3D paths

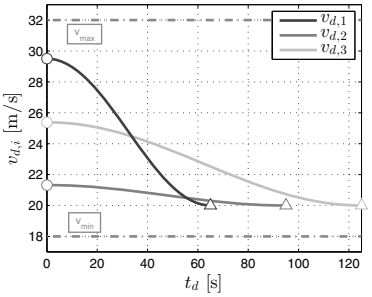

(b) Transition: Desired speed profiles

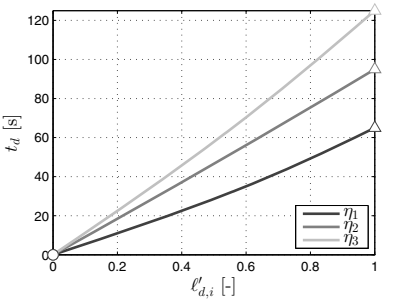

(c) Transition: Coordination maps

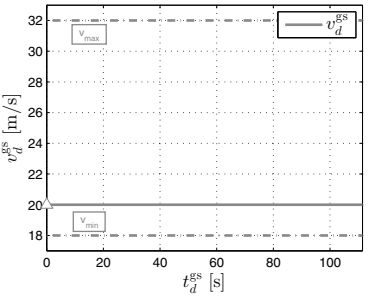

(d) Glide slope: Desired speed profile

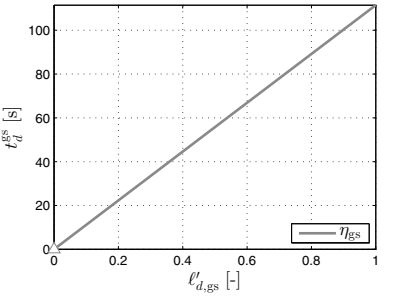

(e) Glide slope: Coordination map

Fig. 11. Sequential auto-landing. Framed 3D spatial paths along with the corresponding desired speed profiles and coordination maps for both the transition trajectories and the glide slope.

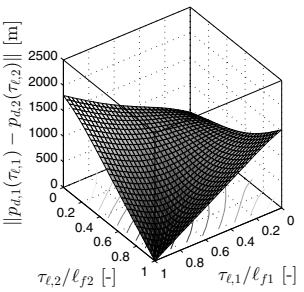

(a) Separation between paths 1 and 2

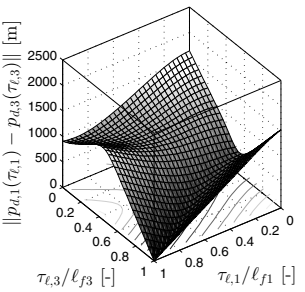

(b) Separation between paths 1 and 3

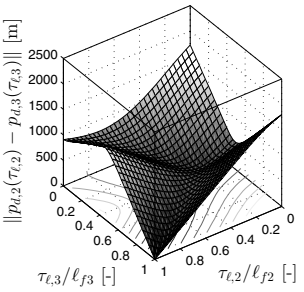

(c) Separation between paths 2 and 3

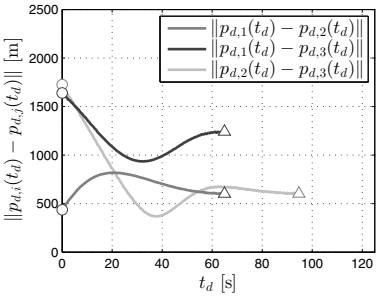

(d) Desired inter-vehicle separation

Fig. 12. Sequential auto-landing. Path separation and desired inter-vehicle separation during the transition phase; the speed profiles ensure deconfliction of the three desired trajectories with a minimum clearance of 350 m.

UAVs start the mission with an initial offset in both position and attitude with respect to the beginning of the transition paths. As can be seen in the figure, the path-following algorithm eliminates this initial offset and steers the UAVs along the corresponding transition paths, while the coordination algorithm ensures that the UAVs reach the glide slope separated by a desired time-interval. The UAVs reach the glide slope at $t = 67.0$ s, $t = 97.0$ s, and $t = 127.0$ s, meeting the desired 30 s inter-vehicle separation. After reaching the glide slope, the path-following algorithm ensures that the UAVs stay on the glide path as the coordination algorithm maintains the safe-guarding separation. The simulation is stopped when the first UAV reaches the end of the glide path.

Figure 14 shows the path-following position and attitude errors, $\boldsymbol{p_{F,i}}$ and $\Psi(\tilde{\boldsymbol{R}}_{\boldsymbol{i}})$, as well as the angular-rate commands, $q_{c,i}$ and $r_{c,i}$, and the rate of progression of the virtual targets along the path $\dot{\ell}_i$. The path-following errors converge to a neighborhood of zero within 40 s.

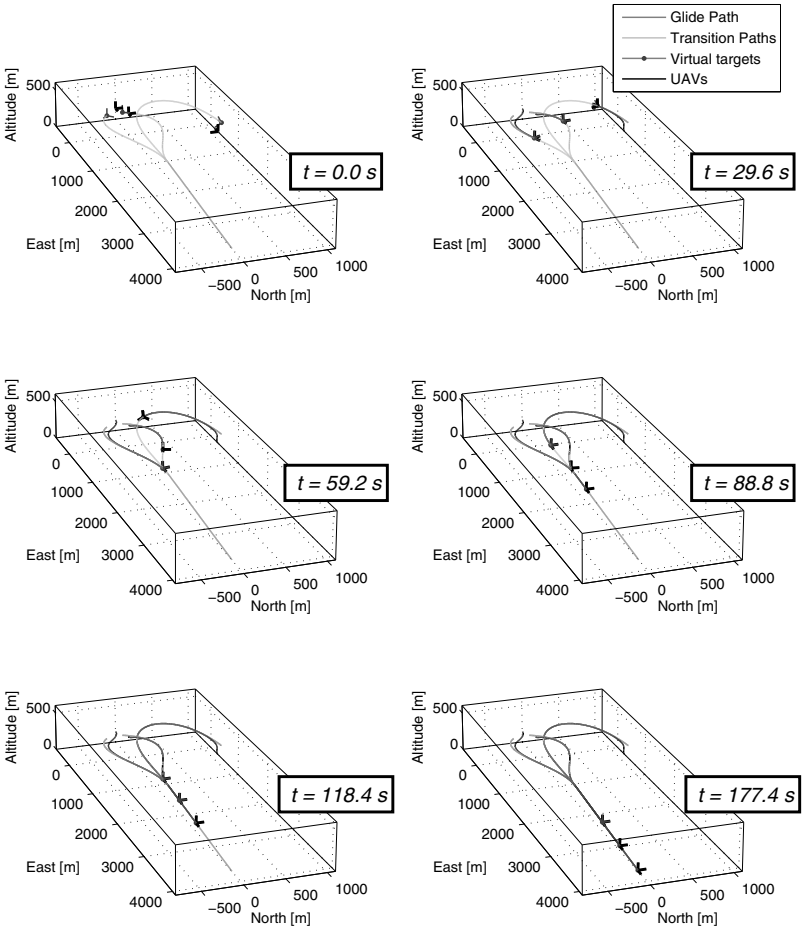

Fig. 13. Sequential auto-landing. The three UAVs arrive at the beginning of the glide path separated by approximately 30 s and maintain this safe-guarding separation as they fly along the glide slope.

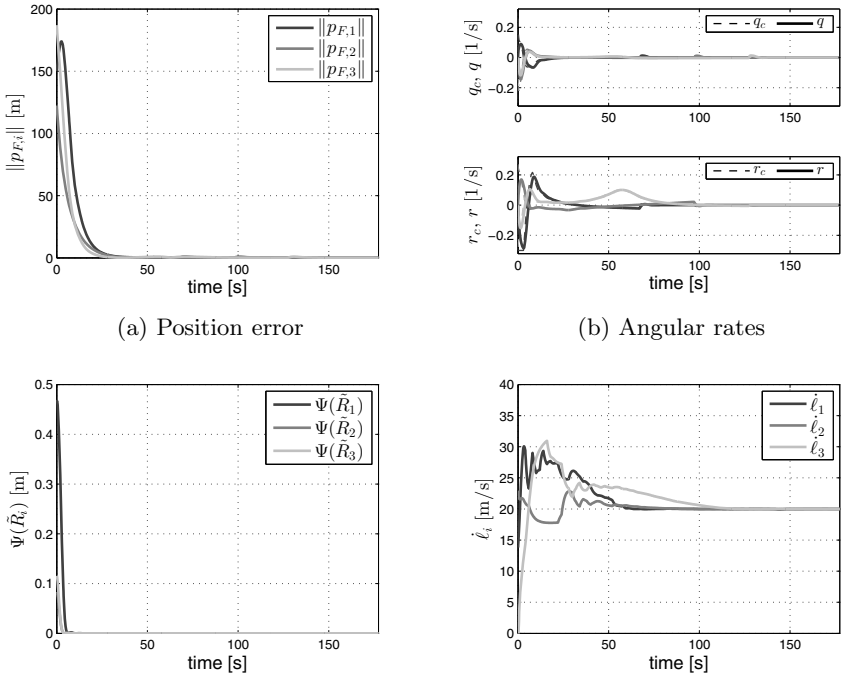

(a) Position error

(b) Angular rates

(c) Attitude error

(d) Progression of the virtual targets

Fig. 14. Sequential auto-landing. The path-following algorithm drives the path-following position and attitude errors to a neighborhood of zero.

The coordination errors $(\xi_i - \xi_j)$ also converge to a neighborhood of zero, while the rate of change of the coordination states $\dot{\xi}_i$ converges to neighborhood of the desired rate $\dot{\xi}_{\text{ref}} = 1$; see Fig. 15. This figure also shows the UAV speeds and the integral states implemented on the follower vehicles. In particular, Figure 15b shows that, after a transient caused by the initial path-following errors as well as the speed corrections introduced by the coordination control law, the speed of each UAV converges to its desired speed and, as the vehicles enter the glide path, their speeds converge to the desired approach speed of 20 m/s. Finally, Figure 16 shows the evolution of the time-varying network topology along with an estimate of the QoS of the network, computed as in (9).

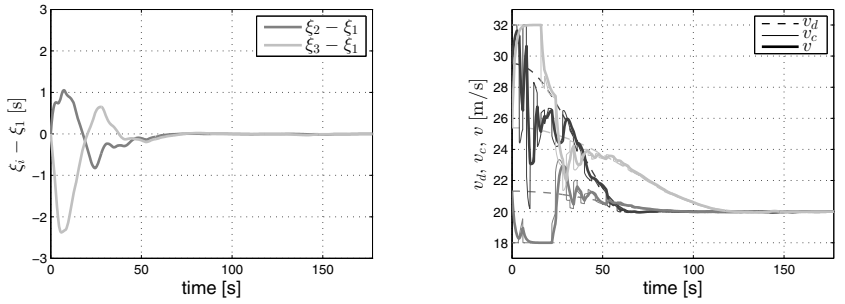

(a) Coordination errors (b) UAV speeds

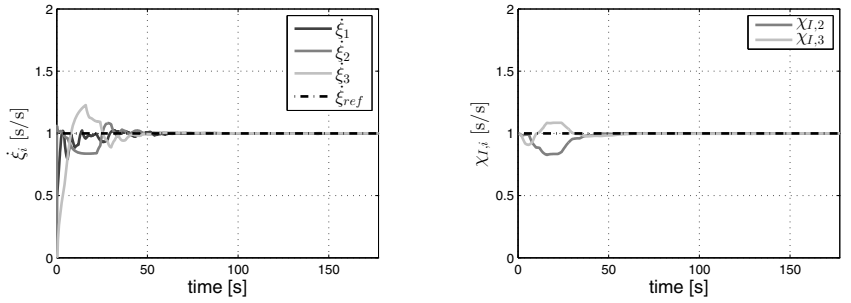

(c) Coordination-state rates (d) Integral states

Fig. 15. Sequential auto-landing. The coordination control law ensures that the coordination errors converge to a neighborhood of zero, thus ensuring trajectory deconfliction, and also that the rate of change of the coordination states evolves at about the desired rate $\dot{\xi}_{\text{ref}} = 1$.

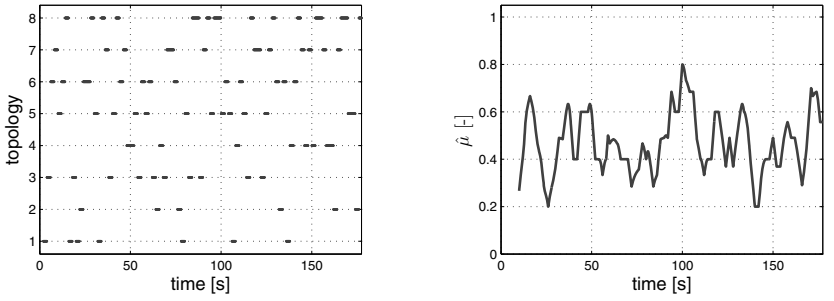

(a) Topology (b) Quality of service

Fig. 16. Sequential auto-landing. At a given time instant, the information flow is characterized by one of the topologies in Fig. 6. The resulting graph is only connected in an integral sense, and not pointwise in time.

6 Conclusions

The paper presented simulation results of two multi-vehicle time-critical missions that exploit a distributed cooperative control framework proposed by the authors in [31]. The simulation study illustrated the efficacy of the algorithms developed and verified the main theoretical claims. Our current research efforts go well beyond concept; in fact, the framework described in this paper has already been tested in a cooperative road-search mission involving two small tactical UAVs equipped with commercial off-the-shelf autopilots. These preliminary flight-test results, which have been reported in [31,36], demonstrate the effectiveness of the proposed theoretical framework in a specific realistic application as well as the feasibility of the onboard implementation of the algorithms.

Acknowledgments. Research was supported in part by Office of Naval Research, Air Force Office of Scientific Research, Army Research Office, European Commission under the FP7 MORPH Project (grant agreement No. 288704), and Fundação para a Ciência e a Tecnologia under the CONAV project (PTDC/EEACRO/113820/2009) and the project PEst-OE/EEI/LA0009/2011.

Appendix: The *hat* and *vee* Maps

The *hat map* $(\cdot)^\wedge : \mathbb{R}^3 \to \mathfrak{so}(3)$ is defined as

$$(\boldsymbol{x})^\wedge = \begin{bmatrix} 0 & -x_3 & x_2 \\ x_3 & 0 & -x_1 \\ -x_2 & x_1 & 0 \end{bmatrix}$$

for $\boldsymbol{x} = [x_1,\ x_2,\ x_3]^\top \in \mathbb{R}^3$. The inverse of the hat map is referred to as the *vee map* $(\cdot)^\vee : \mathfrak{so}(3) \to \mathbb{R}^3$. The reader is referred to [44] for details on these maps.

References

1. Tsitsiklis, J.N., Athans, M.: Convergence and asymptotic agreement in distributed decision problems. IEEE Transactions on Automatic Control 29(1), 42–50 (1984)
2. Sepulchre, R., Paley, D., Leonard, N.: Collective Motion and Oscillator Synchronization. In: Kumar, V., Leonard, N., Stephen Morse, A. (eds.) Cooperative Control. LNCIS, vol. 309, pp. 189–206. Springer, Heidelberg (2005)
3. Jadbabaie, A., Lin, J., Morse, A.S.: Coordination of groups of mobile autonomous agents using nearest neighbor rules. IEEE Transactions on Automatic Control 48(6), 988–1001 (2003)
4. Lin, Z., Francis, B.A., Maggiore, M.: State agreement for continuous-time coupled nonlinear systems. SIAM Journal on Control and Optimization 46(1), 288–307 (2007)
5. Egerstedt, M., Hu, X.: Formation constrained multi-agent control. IEEE Transactions on Robotics and Automation 17(6), 947–951 (2001)
6. Olfati Saber, R., Dunbar, W.B., Murray, R.M.: Cooperative control of multi-vehicle systems using cost graphs and optimization. In: American Control Conference, Denver, CO, pp. 2217–2222 (June 2003)

7. Fax, J.A., Murray, R.M.: Information flow and cooperative control of vehicle formations. IEEE Transactions on Automatic Control 49(9), 1465–1476 (2004)
8. Dunbar, W.B., Murray, R.M.: Distributed receding horizon control for multi-vehicle formation stabilization. Automatica 42(4), 549–558 (2006)
9. Ghabcheloo, R., Pascoal, A.M., Silvestre, C., Kaminer, I.: Coordinated path following control of multiple wheeled robots using linearization techniques. International Journal of Systems Science 37(6), 399–414 (2006)
10. Stevenson, D., Wheeler, M., Campbell, M.E., Whitacre, W.W., Rysdyk, R.T., Wise, R.: Cooperative tracking flight test. In: AIAA Guidance, Navigation and Control Conference, Hilton Head, SC. AIAA 2007-6756 (August 2007)
11. Keviczky, T., Borrelli, F., Fregene, K., Godbole, D., Balas, G.J.: Decentralized receding horizon control and coordination of autonomous vehicle formations. IEEE Transactions on Control System Technology 16(1), 19–33 (2008)
12. Schouwenaars, T., How, J.P., Feron, E.: Decentralized cooperative trajectory planning of multiple aircraft with hard safety guarantees. In: AIAA Guidance, Navigation and Control Conference, Providence, RI. AIAA 2004-5141 (August 2004)
13. McLain, T.W., Beard, R.W.: Coordination variables, coordination functions, and cooperative timing missions. AIAA Journal of Guidance, Control and Dynamics 28(1), 150–161 (2005)
14. Scholte, E., Campbell, M.E.: Robust nonlinear model predictive control with partial state information. IEEE Transactions on Control System Technology 16(4), 636–651 (2008)
15. Kuwata, Y., How, J.P.: Cooperative distributed robust trajectory optimization using receding horizon MILP. IEEE Transactions on Control System Technology 19(2), 423–431 (2011)
16. Fang, L., Antsaklis, P.J., Tzimas, A.: Asynchronous consensus protocols: Preliminary results, simulations and open questions. In: IEEE Conference on Decision and Control, Seville, Spain, pp. 2194–2199 (December 2005)
17. Mesbahi, M.: On state-dependent dynamic graphs and their controllability properties. IEEE Transactions on Automatic Control 50(3), 387–392 (2005)
18. Stilwell, D.J., Bishop, B.E.: Platoons of underwater vehicles. IEEE Control Systems Magazine 20(6), 45–52 (2000)
19. Stilwell, D.J., Bollt, E.M., Roberson, D.G.: Sufficient conditions for fast switching synchronization in time-varying network topologies. SIAM Journal of Applied Dynamical Systems 5(1), 140–156 (2006)
20. Cao, M., Spielman, D.A., Morse, A.S.: A lower bound on convergence of a distributed network consensus algorithm. In: IEEE Conference on Decision and Control, Seville, Spain, pp. 2356–2361 (December 2005)
21. Kim, Y., Mesbahi, M.: On maximizing the second smallest eigenvalue of state-dependent graph Laplacian. IEEE Transactions on Automatic Control 51(1), 116–120 (2006)
22. Mesbahi, M., Hadaegh, F.Y.: Formation flying control of multiple spacecraft via graphs, matrix inequalities, and switching. AIAA Journal of Guidance, Control and Dynamics 24(2), 369–377 (2001)
23. Song, Y.D., Li, Y., Liao, X.H.: Orthogonal transformation based robust adaptive close formation control of multi-UAVs. In: American Control Conference, Portland, OR, vol. 5, pp. 2983–2988 (June 2005)
24. Stipanović, D.M., İnalhan, G., Teo, R., Tomlin, C.J.: Decentralized overlapping control of a formation of unmanned aerial vehicles. Automatica 40(8), 1285–1296 (2004)

25. Skjetne, R., Moi, S., Fossen, T.I.: Nonlinear formation control of marine craft. In: IEEE Conference on Decision and Control, Las Vegas, NV, vol. 2, pp. 1699–1704 (December 2002)
26. Fossen, T.I.: Marine Control Systems: Guidance, Navigation and Control of Ships, Rigs and Underwater Vehicles. Marine Cybernetics, Norway (2002)
27. Pereira, F.L., de Sousa, J.B.: Coordinated control of networked vehicles: An autonomous underwater system. Automation and Remote Control 65(7), 1037–1045 (2004)
28. Ihle, I.A.F.: Coordinated Control of Marine Craft. PhD thesis, Norwegian University of Science and Technology, Trondheim, Norway (September 2006)
29. Ihle, I.A.F., Jouffroy, J., Fossen, T.I.: Robust formation control of marine craft using Lagrange multipliers. In: Pettersen, K.Y., Gravdahl, J.T., Nijmeijer, H. (eds.) Group Coordination and Cooperative Control. LNCIS, vol. 336, pp. 113–129. Springer, Heidelberg (2006)
30. Breivik, M., Hovstein, V.E., Fossen, T.I.: Ship formation control: A guided leader-follower approach. In: IFAC World Congress, Seoul, South Korea (July 2008)
31. Xargay, E., Kaminer, I., Pascoal, A., Hovakimyan, N., Dobrokhodov, V., Cichella, V., Aguiar, A.P., Ghabcheloo, R.: Time-critical cooperative path following of multiple unmanned aerial vehicles over time-varying networks. AIAA Journal of Guidance, Control and Dynamics 36(2), 499–516 (2013)
32. Aguiar, A.P., Pascoal, A.M.: Coordinated path-following control for nonlinear systems with logic-based communication. In: IEEE Conference on Decision and Control, New Orleans, LA, pp. 1473–1479 (December 2007)
33. Ghabcheloo, R., Kaminer, I., Aguiar, A.P., Pascoal, A.M.: A general framework for multiple vehicle time-coordinated path following control. In: American Control Conference, St. Louis, MO, pp. 3071–3076 (June 2009)
34. Ghabcheloo, R., Aguiar, A.P., Pascoal, A.M., Silvestre, C., Kaminer, I., Hespanha, J.P.: Coordinated path-following in the presence of communication losses and delays. SIAM Journal on Control and Optimization 48(1), 234–265 (2009)
35. Kaminer, I., Pascoal, A.M., Xargay, E., Hovakimyan, N., Cao, C., Dobrokhodov, V.: Path following for unmanned aerial vehicles using $\mathcal{L}_1$ adaptive augmentation of commercial autopilots. AIAA Journal of Guidance, Control and Dynamics 33(2), 550–564 (2010)
36. Xargay, E., Dobrokhodov, V., Kaminer, I., Pascoal, A.M., Hovakimyan, N., Cao, C.: Time-critical cooperative control for multiple autonomous systems. IEEE Control Systems Magazine 32(5), 49–73 (2012)
37. Choe, R., Cichella, V., Xargay, E., Hovakimyan, N., Trujillo, A.C., Kaminer, I.: A trajectory-generation framework for time-critical cooperative missions. In: AIAA Infotech@Aerospace, Boston, MA. AIAA 2013-4582 (August 2013)
38. Lapierre, L., Soetanto, D., Pascoal, A.M.: Non-singular path-following control of a unicycle in the presence of parametric modeling uncertainties. International Journal of Robust and Nonlinear Control 16(10), 485–503 (2006)
39. Bishop, R.L.: There is more than one way to frame a curve. The American Mathematical Monthly 82(3), 246–251 (1975)
40. Biggs, N.: Algebraic Graph Theory. Cambridge University Press, New York, NY (1993)
41. Arcak, M.: Passivity as a design tool for group coordination. IEEE Transactions on Automatic Control 52(8), 1380–1390 (2007)
42. Xargay, E., Choe, R., Hovakimyan, N., Kaminer, I.: Multi-leader coordination algorithm for networks with switching topology and quantized information. Automatica 50(3), 841–851 (2014)

43. Aguiar, A.P., Kaminer, I., Ghabcheloo, R., Pascoal, A.M., Xargay, E., Hovakimyan, N., Cao, C., Dobrokhodov, V.: Time-coordinated path following of multiple UAVs over time-varying networks using $\mathcal{L}_1$ adaptation. In: AIAA Guidance, Navigation and Control Conference, Honolulu, HI. AIAA 2008-7131 (August 2008)
44. Lee, T., Leok, M., McClamroch, N.H.: Control of complex maneuvers for a quadrotor UAV using geometric methods on $\mathsf{SE}(3)$. IEEE Transactions on Automatic Control (2010), available online:arXiv:1003.2005v3